

Article

Magnetic Coupling-Based Battery Impedance Measurement Method

Chushan Li ^{1,2}, Junjie Mao ¹, Qiang Wu ¹, Yibo Deng ¹, Jiande Wu ^{1,*}, Wuhua Li ¹ and Xiangning He ¹

¹ College of Electrical Engineering, Zhejiang University, Hangzhou 310081, China; chushan@intl.zju.edu.cn (C.L.); maojunjie@zju.edu.cn (J.M.); wu_qiang@zju.edu.cn (Q.W.); ybdeng@crccap.com (Y.D.); woohualee@zju.edu.cn (W.L.); hxn@zju.edu.cn (X.H.)

² Zhejiang University–University of Illinois at Urbana-Champaign Institute, Zhejiang University, Haining 314400, China

* Correspondence: eewjd@zju.edu.cn

Abstract: The battery impedance is an important indicator of battery health status. In this paper, a magnetic coupling-based impedance measurement method for electrochemical batteries is proposed. Without affecting the energy injection stage, the designed suppression resistance can minimize the influence of the primary circuit response, and the under-damped oscillation waveform containing the battery impedance information can be directly obtained on the primary inductance. The change of the mutual inductance value within a certain range will not affect the measurement results. Therefore, the measurement system has high stability and robustness. By utilizing the discrete Fourier transform (DFT)-based algorithm to calculate the damped oscillation parameters, the battery impedance is accurately derived from the calculated attenuation coefficient and damped oscillation frequency. The accuracy of this method under different coupling parameters is analyzed and verified by simulation and experiment on a Li-ion battery, which could be employed to estimate the state of charge (SOC).

Keywords: battery impedance; magnetic coupling; discrete Fourier transform; damped oscillation; state of charge



Citation: Li, C.; Mao, J.; Wu, Q.; Deng, Y.; Wu, J.; Li, W.; He, X. Magnetic Coupling-Based Battery Impedance Measurement Method. *Energies* **2021**, *14*, 7490. <https://doi.org/10.3390/en14227490>

Academic Editor: Teuvo Suntio

Received: 5 October 2021

Accepted: 5 November 2021

Published: 9 November 2021

Publisher's Note: MDPI stays neutral with regard to jurisdictional claims in published maps and institutional affiliations.



Copyright: © 2021 by the authors. Licensee MDPI, Basel, Switzerland. This article is an open access article distributed under the terms and conditions of the Creative Commons Attribution (CC BY) license (<https://creativecommons.org/licenses/by/4.0/>).

1. Introduction

Electrochemical batteries have become widely used as energy storage devices for electric or hybrid vehicles [1,2], portable electronics [3], and renewable energy storage [4,5]. Therefore, monitoring the battery performance is important to ensure the safety and reliability of the battery-based energy systems.

The battery impedance is widely recognized as an important parameter because it provides useful information on the performance of the battery, including the state of charge (SOC) and other performances. Thus, various electrical battery models have been proposed and reported, which are electrical equivalent models using a combination of voltage sources, resistors, capacitors, and inductors [6–9]. The battery impedance parameters of the equivalent circuit are reflective of electrochemical reactions and transport processes. These factors are affected by the internal thermal condition of the battery, charging current, and ionic concentrations. To identify the battery parameters, electrochemical impedance spectroscopy (EIS) is an attractive method, which is achieved by injecting AC small voltage/current at different frequencies into the battery and measuring its response [8–13]. Thus, the complicated impedance network can be fitted with the impedance spectra. However, EIS requires expensive and cumbersome equipment for a wide range of frequency sweep, making it difficult to be applied in industrial measurements. A cost-effective method is to measure the battery's ohmic resistance at a certain high frequency (typically 1 kHz). The SOC of the battery can be estimated by comparing the measured impedance with long-term collected experimental data [12,13].

Nowadays, the magnetic coupling-based impedance measurement is considered as a significant method, which is used in the inductive power transmission (IPT) system [14–17].

The literature [14–17] proposes a load identification method based on energy injection and energy dissipation. However, the load identification methods in [14–16] do not consider the mutual inductance variation, which is typical for the practical operation of IPT systems with variable magnetic coupling between the primary and secondary coils. The mutual inductance variation is taken into account in [17], but the calculation accuracy is poor. The above measurement method obtains the load impedance value indirectly through the secondary circuit reflection impedance of the coupling circuit, so the accuracy of the measurement result depends on the given mutual inductance value. The data processing method based on the zero-crossing detection and the peak point of the attenuated signal has poor stability and accuracy, especially for the measurement of small resistance, such as Li-ion batteries whose resistance is usually less than 1 Ω .

In this paper, a magnetic coupling-based impedance measurement approach for the electrochemical battery is presented. The proposed measurement approach enables the primary and secondary sides of the coupling circuit to work in different damped oscillation states, so that the secondary side waveform containing the battery impedance information can be directly distinguished by analyzing the waveform characteristics, eliminating the effect of the primary circuit on the measurement result, and reducing the requirement for the accuracy of mutual inductance. The detection method based on magnetic coupling has the electrical isolation capability, and the change of the mutual inductance value within a certain range will not affect the measurement results, so the measurement system has high robustness. By utilizing the discrete Fourier transform (DFT)-based algorithm to calculate the damped oscillation parameters [18], the battery impedance is accurately derived from the calculated attenuation coefficient and damped oscillation frequency. Finally, the accuracy and stability of this method under different coupling parameters are analyzed and verified by simulation and experiment on a Li-ion battery to estimate the state of charge (SOC).

2. Principle of Battery Resistance Measurement

2.1. Simplified Electrical Battery Model

An electrical battery model can be represented with open-circuit voltage (OCV), resistors, capacitors, and inductors of an equivalent circuit, as shown in Figure 1a. The ohmic resistance, R_o , represents the electrolyte resistance. C_{DL} and R_{CT} represent the double layer and charge transfer effects on the electrodes. Warburg impedance Z_W represents the diffusion due to the concentration polarization. The parasitic inductance L_e represents the battery's external/internal connections. OCV represents the battery open-circuit voltage.

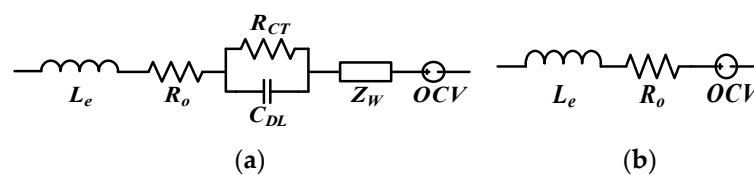


Figure 1. Equivalent circuit of electrical battery model: (a) Full battery impedance model; (b) Simplified battery impedance model.

The battery parameters including R_o , C_{DL} , and R_{CT} are used as the indicators of reflecting the SOC and other battery performances [6–8,10]. To simplify the circuit analysis and reduce the size of the measurement circuit to improve the practicality, 20 kHz was chosen as the measurement frequency. When the measurement frequency is high, the battery impedance model can be simplified by a voltage source in series with a resistor and inductor, as shown in Figure 1b. At this time, the battery equivalent impedance is inductive. According to the study of EIS, the parasitic inductance L_e is usually less than 1 μH [8].

2.2. Measurement Principle

The schematic diagram of the measurement system is shown in Figure 2. M is the mutual inductance. L_1 and L_2 are the loosely coupled inductors with coupling coefficient k ($k \ll 1$), where $L_1 = L_2 = L$, $k = M/\sqrt{L_1L_2} = M/L$. C_1 and C_2 are the compensating capacitors, where $C_1 = C_2 = C$. R_{L1} and R_{L2} are the line resistances, while $R_{L1} = R_{L2} < 2\sqrt{L/C}$. L_x is the battery parasitic inductance, which is usually less than $1 \mu\text{H}$. E is the battery open-circuit voltage. R_x is the battery equivalent resistance, meeting $R_x + R_{L2} < 2\sqrt{L/C}$. R_d is the suppression resistor with a large resistance value, meeting $R_d \gg 2\sqrt{L/C}$. U_{dc} is the DC power supply. u_{L1} is the observed signal, which represents the voltage across the inductor L_1 .

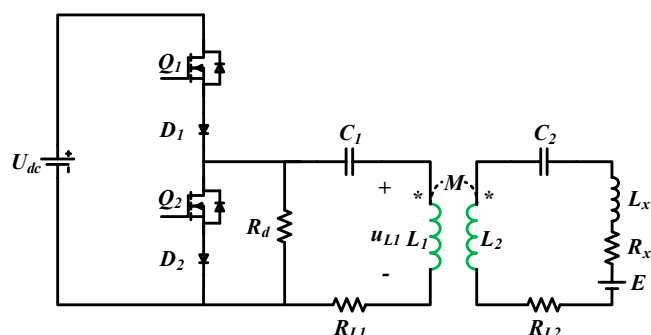


Figure 2. Measurement system.

There are two operation stages in the process of the measurement. The system equivalent circuit in different operation stages is shown in Figure 3.

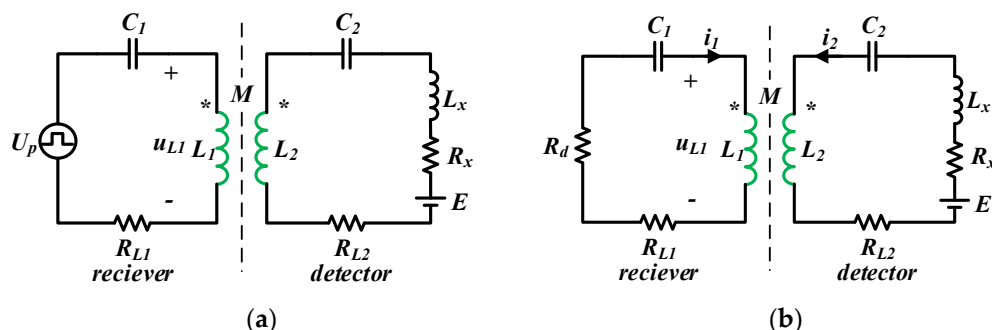


Figure 3. System equivalent circuit in different operation stages: (a) Energy injection stage; (b) Detection stage.

1st stage: Switches Q_1 and Q_2 work in the complementary mode, where the duty cycle is 50% and the switching frequency is at or near the natural resonant frequency ω_0 , which is given by

$$\omega_0 = \frac{1}{\sqrt{LC}}. \tag{1}$$

In this stage, since the circuit works in a resonant state, the large parallel resistance R_d can be ignored. The square voltage source U_p transfers energy to the detector through the mutual inductance. After the circuit goes into the steady state, L_2 and C_2 in the detector are charged; meanwhile, L_1 and C_1 in the receiver are also charged, as shown in Figure 3a.

2nd stage: Switches Q_1 and Q_2 are turned off. The series diodes D_1 and D_2 are used to prevent the current from flowing through the freewheeling diode of the MOS transistor. After that moment, the equivalent circuit is shown in Figure 3b. The circuit operates in free-range response, and the response u_{L1} can be expressed as

$$u_{L1}(t) = L \frac{di_1(t)}{dt} + M \frac{di_2(t)}{dt}. \tag{2}$$

Due to the loose coupling relationship, the current response of the primary and secondary circuit can be recognized as decoupled. The response of the four-order circuit can be simplified to a linear superposition of two independent responses: the primary two-order response and the secondary two-order response.

As shown in Figure 4, the response u_{L1} is composed of the primary self-response, described as u_{L1a} , and the secondary reflected response, which is equivalent to a voltage source $M \cdot di_2/dt$, as described as u_{L1b} .

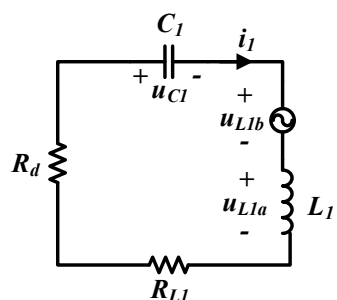


Figure 4. Composition of response u_{L1} .

For the primary self-response, the primary circuit works on the over-damped oscillation, due to

$$R_d + R_{L1} \gg 2\sqrt{L/C}. \tag{3}$$

Assuming the initial condition $u_{c1}|_{t=0} = U_0$ and $i_1|_{t=0} = 0$, thus, u_{L1a} can be described as

$$u_{L1a}(t) = L \frac{di_1(t)}{dt} = A_{11}e^{-\alpha_1 t} + A_{12}e^{-\alpha_2 t} \tag{4}$$

where A_{11} and A_{12} are the voltage amplitude, and α_1 and α_2 are the damping coefficient, which can be derived and simplified as

$$\begin{aligned} b_1 &= \frac{R_d + R_{L1}}{2L} \\ \alpha_1 &= b_1 - \sqrt{b_1^2 - \omega_0^2} \\ \alpha_2 &= b_1 + \sqrt{b_1^2 - \omega_0^2} \\ A_{11} &= \frac{\alpha_2 \alpha_1^2}{\alpha_2 - \alpha_1} LCU_0 \approx \frac{L}{R_d^2 C} U_0 \\ A_{12} &= -\frac{\alpha_1 \alpha_2^2}{\alpha_2 - \alpha_1} LCU_0 \approx -U_0 \end{aligned} \tag{5}$$

Similarly, the secondary circuit works on the under-damped oscillation. The open-circuit voltage of the battery can be regarded as a constant value due to the high measurement frequency. u_{L1b} is derived by

$$u_{L1b}(t) = M \frac{di_2(t)}{dt} = A_2 e^{-\alpha_3 t} \sin(\omega_d t + \varphi) \tag{6}$$

where A_2 is the voltage amplitude, φ is the initial phase angle, α_3 is the damping coefficient, and ω_d is the operating frequency, which can be given by

$$\begin{aligned} \alpha_3 &= \frac{R_x + R_{L2}}{2(L + L_x)} \\ \omega_1 &= \frac{1}{\sqrt{(L + L_x)C}} \\ \omega_d &= \sqrt{\omega_1^2 - \alpha_3^2} \end{aligned} \tag{7}$$

Therefore, the observed signal u_{L1} can be expressed by

$$u_{L1}(t) = A_{11}e^{-\alpha_1 t} + A_{12}e^{-\alpha_2 t} + A_2 e^{-\alpha_3 t} \sin(\omega_d t + \varphi). \tag{8}$$

The battery resistance R_x and battery parasitic inductance L_x can be obtained by the calculation of the damping coefficient α_3 and the operating frequency ω_d in the signal u_{L1b} .

In the under-damped series circuit, with determined inductor L and capacitor C , the parasitic inductance L_x can be derived by (7) and is expressed as

$$L_x = \frac{1}{(\omega_d^2 + \alpha_3^2)C} - L. \quad (9)$$

Similarly, the battery resistance R_x is expressed as

$$R_x = \frac{2\alpha_3}{C(\omega_d^2 + \alpha_3^2)} - R_{L2}. \quad (10)$$

According to (10), the accuracy of the battery resistance depends on the calculation accuracy of the damping coefficient α_3 and the operating frequency ω_d and the given compensating capacitance C .

Additionally, the line resistance R_{L2} can be calculated by the same method in the under-damped circuit composed of the resistance R_{L2} , inductance L , and capacitance C when the battery is not connected.

2.3. Error Signal Analysis

In the measured signal u_{L1} , it can be seen from (8) that the primary self-response u_{L1a} is the possible source of error. Due to $\alpha_2 \gg \alpha_3$, the signal $A_{12}e^{-\alpha_2 t}$ quickly attenuates to nearly zero and has little effect on the measurement accuracy by discarding the previous part of the waveform data. The main source of error is the signal $A_{11}e^{-\alpha_1 t}$. According to (5), when the designed inductance L and compensation capacitance C are determined, the increase in the resistance value R_d is beneficial to suppress the voltage amplitude A_{11} of the error signal and accelerate the decay rate α_2 . However, this does not mean that the larger the suppression resistance R_d , the better. When the circuit is working in the 2nd stage, the primary initial current i_1 is not exactly equal to 0. So, when the resistance R_d is large, voltage spikes will be generated across the resistance to affect the safety and reliability of the circuit.

Figure 5 shows the waveforms of the primary side inductor voltage u_{L1} under different suppression resistance R_d and mutual inductance M . $R_x = 0.2 \Omega$. Other parameters of the measuring circuit are listed in Table 1. As shown in Figure 5a, the observed signal u_{L1} in the 2nd stage is the over-damped oscillation waveform on the primary side when the mutual inductance $M = 0$. Therefore, when the mutual inductance value is 10 μH , the observed voltage u_{L1} in the 2nd stage will introduce the interference error of the primary side, as shown in Figure 5b. By increasing the resistance of the suppression resistor, the response error on the primary side will be suppressed, so that the obtained inductor voltage waveform u_{L1} is a purely under-damped response on the secondary side, as shown in Figure 5c.

Table 1. Simulation parameters.

Parameter Name	Value
$L_1, L_2/\mu\text{H}$	42
$C_1, C_2/\mu\text{F}$	1.5
$R_{L1}, R_{L2}/\text{m}\Omega$	50
$L_x/\mu\text{H}$	0.5
Battery voltage E/V	4.2
Peak input voltage U_{dc}/V	10
Switching frequency f_{sw}/kHz	20
Sampling frequency f_s/MHz	10

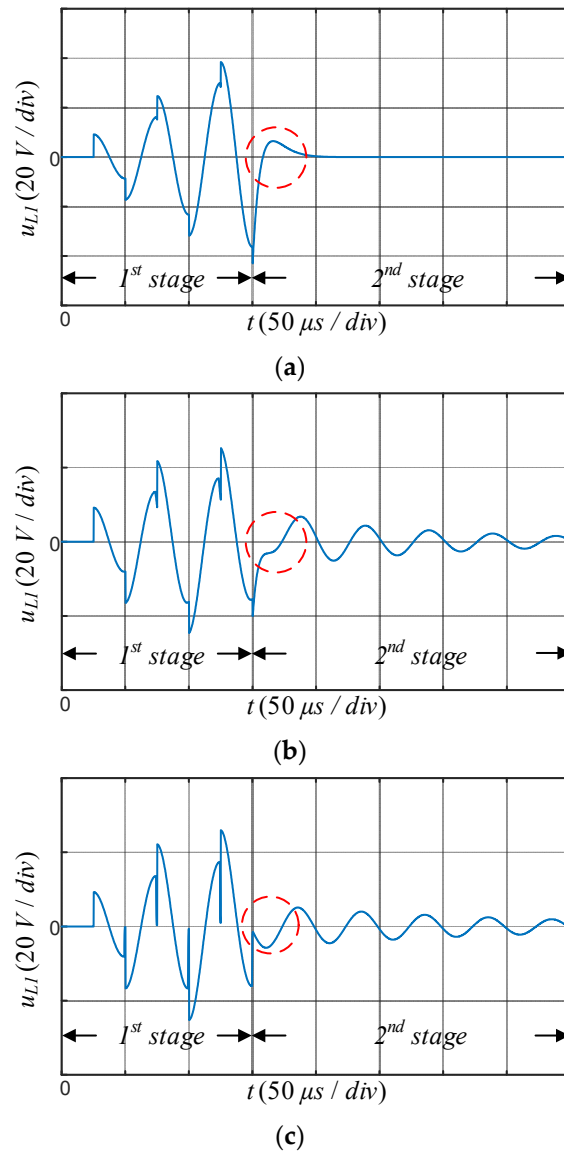


Figure 5. Simulation waveforms of primary side inductor voltage u_{L1} under different suppression resistance R_d and the mutual inductance M . (a) $R_d = 15 \Omega$ and $M = 0$. (b) $R_d = 15 \Omega$ and $M = 10 \mu\text{H}$. (c) $R_d = 1000 \Omega$ and $M = 10 \mu\text{H}$.

3. DFT-Based Estimation of Damped Oscillation Parameters

3.1. DFT-Based Calculation Method

Assuming the observed signal u_{L1} is a pure under-damped wave, and it is defined as

$$x(t) = Ae^{-\beta t} \sin(2\pi f_0 t + \varphi) \quad (11)$$

where A is the maximal amplitude, f_0 is the resonant frequency in hertz, φ is the phase in radians, and β is the decay rate.

The sampling frequency in the measurement system is $f_s = 10 \text{ MHz}$, and the sampling sequence is shown in Figure 6, which is expressed as

$$x[n] = Ae^{-\frac{\delta f_0 n}{f_s}} \sin\left(2\pi \frac{f_0 n}{f_s} + \varphi\right) \quad (12)$$

where δ is the logarithmic decrement, $\delta = \beta/f_0$, $n = 0, 1, \dots, N-1$, and the number of samples is $N = 3000$.

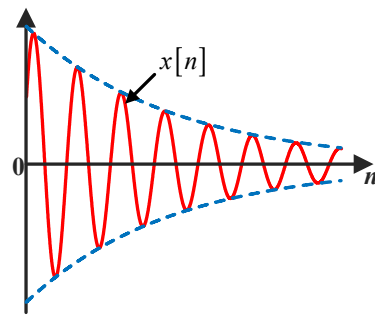


Figure 6. Under-damped waveform.

The DFT of signal (12) is defined as

$$V[k] = \sum_{n=0}^{N-1} x[n]e^{-j\omega_k n} \tag{13}$$

where $\omega_k = (2\pi/N)k$, $k = 0, 1, 2, \dots, N - 1$.

Its angular frequency ω_d/f_s lies either between the DFT bins ω_K and ω_{K+1} or ω_K and ω_{K-1} , where the DFT bin for ω_K has the highest magnitude.

By using the Bertocco-Yoshida algorithm [18], the first-order difference ratio of the DFT spectrum can be described as follows:

$$R = \frac{V[K - 1] - V[K]}{V[K] - V[K + 1]} \tag{14}$$

Then

$$\lambda = e^{j\omega_K} \frac{r - R}{re^{-j2\pi/N} - Re^{j2\pi/N}} \tag{15}$$

$$r = \frac{-e^{-j\omega_K} + e^{-j\omega_{K-1}}}{-e^{-j\omega_{K+1}} + e^{-j\omega_K}} \tag{16}$$

and the decay rate β and resonant frequency f_0 are expressed as

$$\begin{aligned} \beta &= -\text{Re}\{\ln(\lambda)\} \cdot f_s \\ f_0 &= \text{Im}\{\ln(\lambda)\} \cdot f_s / 2\pi \end{aligned} \tag{17}$$

3.2. Constraint Range of Measurement Object

Although the proposed method is suitable for calculating the decay rate and resonant frequency of the under-damped oscillation waveform, the logarithmic decrement has certain limitations on the calculation accuracy.

The estimation accuracy for test signals with $f_0 = 20.1$ kHz is analyzed under different values of δ . As shown in Figure 7, the calculation accuracy of the decay rate β and resonant frequency f_0 decreases as the logarithmic decrement δ increases. Especially when $\delta > 1$, the accuracy of the decay rate β decreases significantly. Therefore, to guarantee that the calculating accuracy of the decay rate β and resonant frequency f_0 is higher than 98%, δ needs to be restrained within 1.

Comparing (12) and (6), δ can be expressed as

$$\delta = \frac{2\pi\alpha_3}{\omega_d} = \frac{2\pi \frac{R_x + R_{L2}}{2(L + L_x)}}{\sqrt{\frac{1}{(L + L_x)C} - \left[\frac{R_x + R_{L2}}{2(L + L_x)}\right]^2}} = \frac{2\pi}{\sqrt{\frac{4(L + L_x)}{(R_x + R_{L2})^2 C} - 1}} = \frac{2\pi}{\sqrt{4Q^2 - 1}} \tag{18}$$

where Q is the quality factor of the secondary circuit.

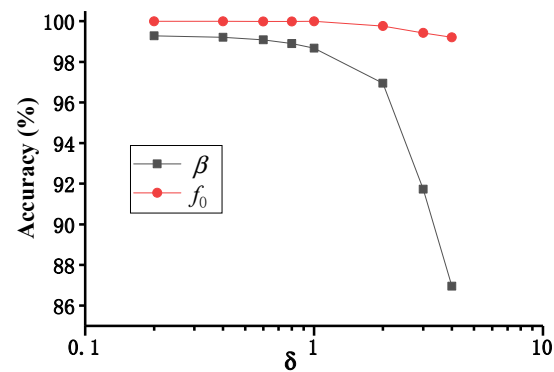


Figure 7. Calculation accuracy of decay rate β and resonant frequency f_0 .

To ensure that the measurement method based on the DFT algorithm has high accuracy, the quality factor of the circuit needs to be large. This provides guidelines for the circuit parameter design.

Due to $\delta < 1$, the measurement range of battery internal resistance can be derived as

$$R_x < 0.314 \sqrt{\frac{L + L_x}{C}} - R_{L2} \quad (19)$$

According to (19), under the limitation of the accuracy of the DFT algorithm, the measurement range of the battery resistance depends on the designed circuit parameters L and C . This condition is much stronger than the conditions that make the circuit work in the under-damped oscillation state.

3.3. Detection Error of Battery Resistance

Although [18] shows that this method has high accuracy under the interference of Gaussian white noise, whether it has high accuracy for the source of error in this letter requires simulation and experimentation to verify.

Define γ_1 as an estimation of the relative magnitude of the error signal, which is expressed as $\gamma_1 = A_{11}/A_2$.

Define γ_2 as the ratio of the damping coefficient, which is expressed as

$$\gamma_2 = \frac{\alpha_1}{\alpha_3} \approx \frac{2(L + L_x)}{C(R_x + R_{L2})(R_d + R_{L1})} \quad (20)$$

The size of γ_1 and γ_2 is the main parameter to measure the effect of the error signal, which is related to the mutual inductance M and the primary side resistor R_d . By selecting the appropriate circuit parameters, $\gamma_2 \ll 1$. $R_d = 10 \text{ k}\Omega$. Thus, the measurement accuracy of the resistance R_x can be analyzed by using M as the variable. The calculated resistance is expressed by R_m , and the measurement error ε is expressed by $\varepsilon = R_m - R_x$. Other parameters of the measuring circuit are listed in Table 1.

As shown in Figure 8, this simulation result shows the changes in measurement error ε , where the mutual inductance values are $2 \text{ }\mu\text{H}$, $5 \text{ }\mu\text{H}$, $10 \text{ }\mu\text{H}$, and $20 \text{ }\mu\text{H}$. When the battery resistance R_x changes from 0 to $1000 \text{ m}\Omega$, the measurement error ε approximates a linearly decreasing process and the variation range of the measurement error does not exceed $12 \text{ m}\Omega$. The change of the mutual inductance value within a certain range from 5 to $2 \text{ }\mu\text{H}$ has a little influence on the measurement results. The simulation result shows that the proposed method is also suitable for measurement occasions with high coupling factors when the mutual inductance value is $20 \text{ }\mu\text{H}$.

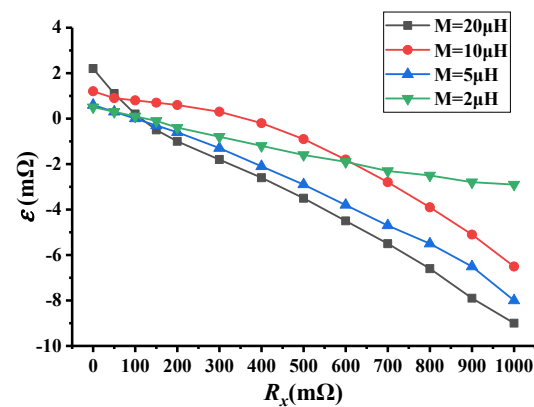


Figure 8. Detection error curve.

4. Experiment Result

In this section, the experimental platform is demonstrated in Figure 9. In the experimental system, the stm32f407 was selected as a controller of the load detection control system, and MOSFETs (Vishay, America) (SI2327DS and SI2324DS) were selected as the switch devices of the half-bridge inverter circuit. The high-speed sampling chip AD9220 was selected to sample the inductor voltage at 10 MHz. The platform can be used to test the resistance of batteries. The ambient temperature during the battery resistance test is 20 °C.

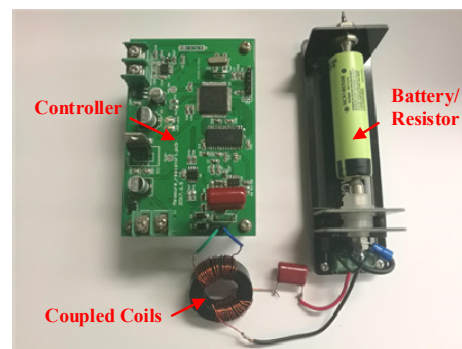


Figure 9. Experimental platform.

To verify the accuracy and practicality of the proposed method, experiments are conducted to detect the electrical network formed by series connection of standard resistors, inductors, and voltage source. The standard resistors have different resistance values, the inductance value is 1 μH , and the voltage source is 4.2 V. As shown in Figure 10, for standard resistor resistance R_x between 100 and 500 m Ω , the accuracy rate of the load detection is more than 98%.

To examine the effects of the SOC value on the resistance of the Li-ion battery, the measurement is performed at different SOC values, ranging from 100% to 0%, for different C-rates (1/4, 1/2 and 1C) when the frequency of the power converter is at 20 kHz. The line resistance can be measured by shorting the secondary circuit when the battery is not connected. This part can be subtracted from the final measured impedance to obtain the battery resistance. The contact resistance is included in the final measured resistance, but this does not affect the study of the trend of battery resistance as the SOC changes.

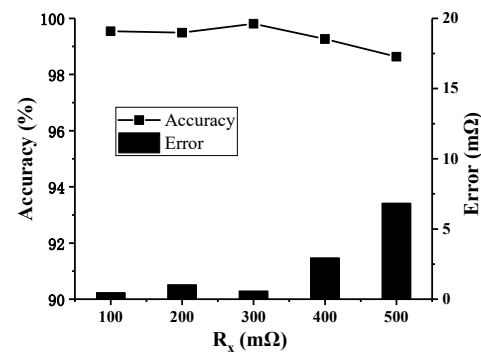


Figure 10. Detection accuracy and error.

It can be observed in Figure 11 that the overall trend of the internal resistance of the battery is to decrease first and then increase as the SOC decreases. Among three different discharge rates, the battery resistance at 1C is the largest. The battery resistance varies little when the SOC decreases from 100% to 20%, and the battery resistance increases significantly when the SOC decreases from 20% to 0%. Therefore, this measurement method is suitable for the detection of deep battery discharge.

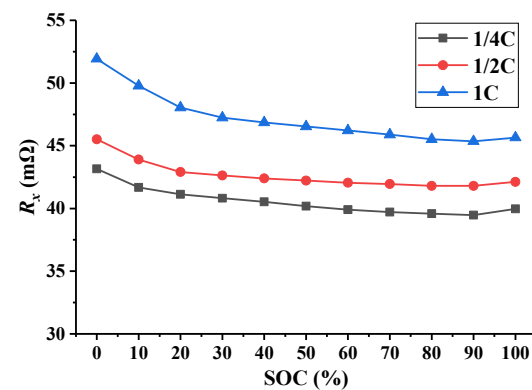


Figure 11. Battery resistance at various SOC values and C-rates.

5. Conclusions

This paper has presented a magnetic coupling-based resistance measurement method for electrochemical batteries. The proposed measurement circuit enables the primary and secondary sides of the coupling circuit to work in different damped oscillation states so that the secondary side waveform containing the battery impedance information can be directly distinguished by analyzing the waveform characteristics, eliminating the effect of the primary circuit on the measurement result and reducing the requirement for accuracy of mutual inductance.

By utilizing the discrete Fourier transform (DFT)-based algorithm to calculate the damped oscillation parameters, the battery impedance is accurately derived from the calculated attenuation coefficient and damped oscillation frequency. The measurement range of the battery resistance is given according to the calculation accuracy of the DFT algorithm.

It can be seen through simulation that this measurement method has high accuracy. The change of the circuit mutual inductance value within a certain range will not affect the measurement results.

The standard resistance has been measured repeatedly by experiments to prove that the method has high accuracy, and the experiment confirms the change of battery resistance under different SOC values and different C-rates, which can be used to infer the SOC of a Li-ion battery.

Author Contributions: Conceptualization, J.W.; Data curation, Q.W.; Resources, Y.D. and X.H.; Supervision, C.L. and W.L.; Writing—original draft, J.M. All authors have read and agreed to the published version of the manuscript.

Funding: This research received no external funding.

Institutional Review Board Statement: Not applicable.

Informed Consent Statement: Not applicable.

Conflicts of Interest: The authors declare no conflict of interest.

References

1. Yilmaz, M.; Krein, P.T. Review of Battery Charger Topologies, Charging Power Levels, and Infrastructure for Plug-In Electric and Hybrid Vehicles. *IEEE Trans. Power Electron.* **2013**, *5*, 2151–2169. [[CrossRef](#)]
2. Hsu, R.C.; Liu, C.; Chan, D. A Reinforcement-Learning-Based Assisted Power Management with QoR Provisioning for Human-Electric Hybrid Bicycle. *IEEE Trans. Ind. Electron.* **2012**, *8*, 3350–3359. [[CrossRef](#)]
3. Brush, L.C. Portable devices emerging power solutions. *EDN Power Supplement*, November 2003; 23–26.
4. Velasco de la Fuente, D.; Trujillo Rodríguez, C.L.; Garcerá, G.; Figueres, E.; Ortega Gonzalez, R. Photovoltaic Power System with Battery Backup with Grid-Connection and Islanded Operation Capabilities. *IEEE Trans. Ind. Electron.* **2013**, *4*, 1571–1581. [[CrossRef](#)]
5. Teleke, S.; Baran, M.E.; Huang, A.Q.; Bhattacharya, S.; Anderson, L. Control Strategies for Battery Energy Storage for Wind Farm Dispatching. *IEEE Trans. Energy Convers.* **2009**, *3*, 725–732. [[CrossRef](#)]
6. Chen, M.; Rincon-Mora, G.A. Accurate electrical battery model capable of predicting runtime and I–V performance. *IEEE Trans. Energy Convers.* **2006**, *2*, 504–511. [[CrossRef](#)]
7. Einhorn, M.; Conte, F.V.; Kral, C.; Fleig, J. Comparison, Selection, and Parameterization of Electrical Battery Models for Automotive Applications. *IEEE Trans. Power Electron.* **2013**, *3*, 1429–1437. [[CrossRef](#)]
8. Li, S.; Wang, B.; Peng, H.; Hu, X. An electrochemistry based impedance model for lithium ion batteries. *J. Power Sources* **2014**, *258*, 9–18. [[CrossRef](#)]
9. Lee, Y.; Park, S.; Han, S. Online Embedded Impedance Measurement Using High-Power Battery Charger. *IEEE Trans. Ind. Appl.* **2015**, *1*, 498–508. [[CrossRef](#)]
10. Howey, D.A.; Mitcheson, P.D.; Yufit, V.; Offer, G.J.; Brandon, N.P. Online Measurement of Battery Impedance Using Motor Controller Excitation. *IEEE Trans. Veh. Technol.* **2014**, *6*, 2557–2566. [[CrossRef](#)]
11. Buller, S.; Thele, M.; De Doncker, R.W.A.A.; Karden, E. Impedance-based simulation models of supercapacitors and Li-ion batteries for power electronic applications. *IEEE Trans. Ind. Appl.* **2005**, *3*, 742–747. [[CrossRef](#)]
12. Huang, W.; Abu Qahouq, J.A. An Online Battery Impedance Measurement Method Using DC–DC Power Converter Control. *IEEE Trans. Ind. Electron.* **2014**, *11*, 5987–5995. [[CrossRef](#)]
13. Carkhuff, B.G.; Demirev, P.A.; Srinivasan, R. Impedance-Based Battery Management System for Safety Monitoring of Lithium-Ion Batteries. *IEEE Trans. Ind. Electron.* **2018**, *8*, 6497–6504. [[CrossRef](#)]
14. Dai, X.; Sun, Y.; Tang, C.; Wang, Z.; Su, Y.; Li, Y. Dynamic parameters identification method for inductively coupled power transfer system. In Proceedings of the IEEE International Conference on Sustainable Energy Technologies, Kandy, Sri Lanka, 6–9 December 2010; pp. 1–5.
15. Hu, S.; Liang, Z.; Wang, Y.; Zhou, J.; He, X. Principle and Application of the Contactless Load Detection Based on the Amplitude Decay Rate in a Transient Process. *IEEE Trans. Power Electron.* **2017**, *11*, 8936–8944. [[CrossRef](#)]
16. Wang, Z.; Li, Y.; Sun, Y.; Tang, C.; Lv, X. Load Detection Model of Voltage-Fed Inductive Power Transfer System. *IEEE Trans. Power Electron.* **2013**, *11*, 5233–5243. [[CrossRef](#)]
17. Su, Y.; Zhang, H.; Wang, Z.; Hu, A.P.; Chen, L.; Sun, Y. Steady-state load identification method of inductive power transfer system based on switching capacitors. *IEEE Trans. Power Electron.* **2015**, *11*, 6349–6355. [[CrossRef](#)]
18. Duda, K.; Magalas, L.B.; Majewski, M.; Zielinski, T.P. DFT-based Estimation of Damped Oscillation Parameters in Low-Frequency Mechanical Spectroscopy. *IEEE Trans. Instrum. Meas.* **2011**, *11*, 3608–3618. [[CrossRef](#)]